

Transformer-based segmentation of adnexal lesions and ovarian implants in CT images

**Authors List:**

Aneesh P. Rangnekar, PhD, Department of Medical Physics, Memorial Sloan Kettering Cancer Center  
Kevin M. Boehm, MD, PhD, Computational Oncology, Department of Epidemiology and Biostatistics, Memorial Sloan Kettering Cancer Center  
Emily A. Aherne\*, MD, Department of Radiology, Memorial Sloan Kettering Cancer Center  
Ines Nikolovski\*, MD, Department of Radiology, Memorial Sloan Kettering Cancer Center  
Natalie Gangai, MPH, Department of Radiology, Memorial Sloan Kettering Cancer Center  
Ying Liu, MD, MPH, Department of Medical Oncology, Memorial Sloan Kettering Cancer Center  
Dimitry Zamarin\*, MD, PhD, Department of Medical Oncology, Memorial Sloan Kettering Cancer Center  
Kara L. Roche, MD, MSc, FACOG, Department of Surgical Oncology, Memorial Sloan Kettering Cancer Center  
Sohrab P. Shah, PhD, Computational Oncology, Department of Epidemiology and Biostatistics, Memorial Sloan Kettering Cancer Center  
Yulia Lakhman, MD, Department of Radiology, Memorial Sloan Kettering Cancer Center  
Harini Veeraraghavan, PhD, Department of Medical Physics, Memorial Sloan Kettering Cancer Center

\* relevant work performed while at Memorial Sloan Kettering Cancer Center

**Acknowledgments:** We thank the MSK MIND consortium and the NIH National Cancer Institute MSK Cancer Center Support Grant P30CA008748

**Data Sharing Statement:** The evaluation data was derived from the The Cancer Imaging Archive: <https://www.cancerimagingarchive.net>. The institutional data is not currently permitted to be released due to legal and ethical implications.

**Purpose:** To evaluate the efficacy of transformer-backbone based deep learning models on segmenting high-grade serous ovarian carcinoma in contrast-enhanced CT images.

**Materials and Methods:** Two fully automated segmentation models with a transformer-backbone, specifically a hierarchical transformer backbone, were trained and evaluated for two most common disease sites for ovarian cancer, namely adnexal lesions and omental implants. This retrospective analysis used 245 institutional contrast-enhanced CT image scans for training the models and evaluated them on 71 multi-institutional TCIA image scans. Performance was assessed under partially labeled and completely labeled scenarios using metrics including Dice similarity coefficient metric (DSC), average symmetric surface distance (ASSD), precision, and recall. Organ overlaps were computed using the open-source TotalSegmentator model, and all metrics were compared using paired two-sided Wilcoxon signed rank tests.

**Results:** Both segmentation models (SMIT and Swin UNETR) achieved a DSC exceeding 0.75 for adnexa lesions and omental implants, and SMIT showed higher precision ( $p = 0.002$ ) than Swin UNETR for specifically detecting tumors in the adnexa. SMIT also resulted in a comparably smaller portion of organ overlaps (in small bowel, colon, and the urinary bladder) than Swin UNETR.

**Conclusion:** The paper demonstrated the first application of transformer-based segmentation models for ovarian cancer analysis. Two models were investigated in this paper and the research yielded promising results with high Dice accuracy scores exhibiting their efficacy in accurately delineating tumors.

## Introduction

High-grade serous ovarian carcinoma (HGSOC) accounts for most ovarian cancer related deaths [1]. Conventional treatment consists of cytoreductive surgery and chemotherapy wherein complete surgical resection yields the best oncologic outcome [2-4]. Despite maximal surgical effort, most patients recur and develop chemotherapy resistant disease [5]. Poor prognosis is underpinned by the loss of DNA repair mechanisms, resulting in high genomic heterogeneity, early clonal evolution, and rapid onset of chemo-resistance [6-11]. Besides genomic drivers, spatial variations in tumor microenvironment exert key selective pressures that shape the evolutionary trajectory and disease dynamics [12]. Since most patients with HGSOC manifest with high volume multi-site disease, multi-region analysis (primary tumor and peritoneal implants) is essential to accurately capture tumor diversity and identify key determinants of prognosis and treatment response.

Detailed tumor segmentation is a labor-intensive manual task that is especially challenging in high volume multi-site tumors like HGSOC. Most healthcare institutions have picture archiving and communication systems (PACS) that store millions of imaging studies. However, most examinations are not suitable for machine learning (ML) automation because they lack necessary labels and annotations [13]. Large, well-annotated, and preferably multi-stream data sets are essential for the development and implementation of ML applications including volumetric tumor delineation, parallel tracking of multiple lesions, phenotyping of genomic tumor heterogeneity, and integrated diagnostics. Semi/automated tumor segmentation with deep learning techniques can accelerate downstream computational analyses of multi-modal data and augment the discovery of non-invasive biomarkers.

Deep learning methods have demonstrated the capability to segment cancers in the lung [14], adrenal masses [15], pancreas [16], as well as colorectal liver metastases [17]. However, such methods are restricted to individual disease sites or tumor types that have distinct imaging appearance. One prior work [18] studied the problem of segmenting hypodense perihepatic and perisplenic ovarian metastases using a level set-based region growing approach. However, segmentation of primary and metastatic disease occurring in different sites is challenging due to the highly heterogeneous CT imaging appearance, such as presence of cystic and non-cystic components within a single tumor site as well as highly irregular shapes of ovarian cancers. A more recent work used deep learning-based approach using a convolutional network built on the nnU-Net architecture to segment primary tumors and omental implants from CT scans [19] using a fully supervised learning framework. Our approach extends these prior works by employing self-supervised pretrained transformer models and studied the capability of training these methods in the presence of partial annotations, while utilizing a human-in-the-loop scenario for generating volumetric segmentation of omental implants.

We employed transformers because these are more accurate than convolutional networks for segmenting tumors and organs [20-22], due to their ability to efficiently and effectively capture both local and global image context without losing image resolution. Convolutional architectures must perform successive pooling to extract features encompassing larger spatial context and inevitably lose resolution that reduces accuracy. Relatedly, advances in self-supervised learning (SSL) enables models to leverage large and unlabeled image sets that are unrelated to downstream tasks and learn useful feature representations such that fine-tuning can be performed on relatively small task-specific labeled datasets [23,24]. Hence, we utilized two pretrained transformer models, one called self-distilled masked image transformer (SMIT) [23] and the other called Swin UNETR [25] for segmenting adnexal tumors and omental implants on contrast-enhanced computed tomography (CECT) images in patients with advanced ovarian cancer.

Importantly, for the first time, we studied whether transformer-based AI models can be trained and improved in an AI-assisted radiologist annotation framework. We used a framework, wherein an AI model trained with a set of partially labeled examples was used to assist a radiologist to refine segmentations on missing slices with reduced effort than carefully annotating every single image slice. AI-assisted labeling was performed by verifying/editing pseudo segmentations by an expert radiologist. We measured segmentation accuracy of models trained with (1) full and partially labeled images as well as (2) full and AI-assisted labeled images.

## Materials and Methods

### Study Design, Patients, and Controls

This retrospective analysis was approved by the local institutional review board, with a waiver for written informed consent, and was compliant with the Health and Insurance Portability and Accountability Act. The public domain dataset from the open source the Cancer Imaging Archive (TCIA) was used compliant with TCIA policies, such as maintaining participants' privacy, accessing the data securely, and publication guidelines.

### Training and validation dataset

The training dataset consisted of 245 institutional CECT scans of patients diagnosed with Stage II to IV HGSOE [27]. These scans were acquired using different scanner manufacturers including GE (n = 170) and the rest (n = 75) from a mix of Siemens, Philips, and Toshiba. Majority of the CECT scans were acquired with a peak kilovoltage of 120 KVp, and a range of 80 to 140 KVp and reconstructed with standard convolution kernels (5mm thickness; range of 2.5mm to 5mm). Segmentation models were trained with 75% (n = 183) of the data and validated on 25% (n = 62 scans) to select the model for independent testing. Figures 1A and 1B show the overall training and testing workflow.

The dataset contained fully annotated adnexal masses and partially annotated omental implants, wherein delineations were available either in some slices or in part of the tumors occurring in a single slice. Partial delineation was performed for omental implants because these lesions are often multifocal and are more manually demanding to segment.

AI-assisted model training was performed using 3-fold stratified cross validation by balancing the prevalence of omental implants and adnexal masses in all folds. Specifically, an independent AI model called multiple resolution residual network (MRRN) [26] was trained on 2 folds with the remaining fold set aside for validation in 3-fold cross validation (Figure 1C). The set aside validation fold was used to generate "pseudo" segmentations by the AI model (MRRN), which following the verification by a radiologist constituted the AI-assisted labeled set.

### Testing dataset

Publicly available multi-institutional ovarian-TCIA dataset (n = 71) was used for independent testing [28]. Radiologists XX and XY generated segmentations of all visible adnexal masses and omental implants. Majority of the scans were acquired using GE (n = 43) while the remaining were a mixture of Siemens, Philips, and Toshiba scanners (n = 28). The summary statistics for the datasets is provided in Table 1.

### Deep learning architecture and training details

SMIT model, which was previously developed for abdominal organ segmentations, was the default network used in the analysis [23]. SMIT's performance was compared against Swin UNETR [25], which also uses a pretrained transformer model. Publicly available models and weights for these two methods as provided by the respective authors in the GitHub repositories were used as is and then fine-tuned on our dataset to achieve the best performance possible using identical training, validation, and testing datasets.

Briefly, both networks were created using the hierarchical Swin transformer [29] backbone to encode image features using multi-head self-attention and then followed by a 3D-U-Net [30] style decoder to generate volumetric segmentation. Hence, both models were architecturally identical. SMIT and Swin UNETR networks differed in the pretext tasks used for SSL pre-training. Whereas Swin UNETR used masked volume inpainting, rotation invariance, and contrastive coding pretext tasks, SMIT used masked image prediction, masked patch token self-distillation, and global image token self-distillation to extract both local and global image feature semantics using a self-distilled framework consisting of a student and identical exponentially moving average teacher network [32].

Both networks were fine-tuned on identical institutional datasets by minimizing a combination of Dice and cross entropy loss. Specifically, the encoders were initialized with the model weights provided publicly by the respective publications; the U-Net model used for segmentation was initialized with random weight and trained from scratch. Because the tumors in the adnexa and the omentum have distinctly different appearance and occur in different spatial locations, these tumors were treated as two separate classes for network training. Consistent data preprocessing, augmentations, learning rate

schedule, epochs, and loss functions were used to maintain fairness in model evaluations. We performed sliding window inference with 50% Gaussian overlap to segment a full 3D CECT scan with varying fields of view. Summary statistics of the model training and evaluation hyperparameters are provided in Table 2.

### **AI-assisted labeling**

The steps in AI-assisted labeling were as follows: (1) train a 2D MRRN [26] on the individual cross validation folds to generate pseudo-segmentations on the remaining validation fold, (2) present cases with Dice similarity coefficient (DSC) accuracy for individual tumors compared to original expert delineations below 0.5 for expert review, (3) perform radiologist-verified AI segmentations with edits by a radiologist where required. Any false tumor detections were erased with a single click. This collaborative synergy between the AI model and a radiologist was deployed for a single annotation revision cycle.

The 2D MRRN model was used to generate pseudo labels and assist in radiologist editing to ensure unbiased delineations for training and evaluating the transformer networks. A 2D model was chosen to utilize a larger number of examples available from individual slices to train the model with the initial full and partially labeled training dataset. This model was optimized using a combination of Dice and cross entropy loss applied to cropped and Gaussian smoothed images to provide a closer spatial context to the tumors of interest and reduce the impact of image noise, respectively.

### **Evaluation metrics and statistical analysis**

The tumor segmentations produced by the transformer networks were compared to manual delineations as reference. The accuracy was measured using Dice similarity coefficient (DSC), average symmetric surface distance (ASSD), precision, and recall metrics. DSC and ASSD were computed for detected tumors (DSC  $\geq$  0.5 with respect to the expert delineation). Precision and recall rate were used to quantify the tumor detection accuracy for all the segmented tumors. All metrics, except ASSD, range in the values from 0 (worst) to 1 (best). Manual effort in editing pseudo labels to produce AI-assisted segmentations was measured using added path length (APL) metric(31). In addition, organs where false tumor segmentations occurred were assessed by computing the overlap of such tumor segmentations with the individual abdominal organs (e.g., small bowel, colon, urinary bladder). Organ segmentations were produced by utilizing automated organ segmentations generated using the open-source TotalSegmentator model [33]. TotalSegmentator delineations were used as is because this model has been published as a general-purpose segmentation model.

Bland Altman plots were computed to measure the difference in the segmented versus manually delineated tumor volumes. Statistical comparisons between SMIT and Swin UNETR models were performed using paired, two-sided Wilcoxon signed rank tests at 95% confidence level. Only p-values lower than 0.05 were considered significant.

## Results

### Model Performance Comparisons

SMIT and Swin UNETR achieved an average DSC accuracy exceeding 0.75 for both adnexa and omental implants when trained with a combination of full and AI-assisted radiologist delineations. Segmentations produced by the two models for representative cases are shown in Figure 2. Segmentations produced by both models were statistically similar in terms of DSC and ASSD for omental implants ( $p = 0.094$ ). Both models also had a similar recall for detecting adnexal masses (Supplementary Figure S1). However, SMIT achieved a significantly higher precision ( $p = 0.002$ ) for detecting tumors in the adnexa.

Further analysis of differences in segmented tumor volumes using Bland Altman plots showed that Swin UNETR resulted in over-segmentations compared to SMIT (Figure 3). Swin UNETR showed a larger spread in the DSC and reduced precision than the SMIT model on case-wise analysis of accuracy. Swin UNETR also had lower precision and recall for omental implants compared to SMIT (Supplementary Figure S2).

Analysis of the impact of tumor detection threshold on the accuracy showed that SMIT achieved consistently higher DSC and precision, and lower ASSD but similar recall as Swin UNETR for both tumor types (Supplementary Figure S3 and S4). Sources of poor models' performance, for the omental implants occurred due to (1) missed segmentations (Supplementary Figure S5), (2) segmentations generated in slices adjacent to those containing confirmed tumor segmentations (Supplementary Figure S6), and (3) incorrect assignment of the segmentation labels (adnexa versus omentum and vice versa) (Supplementary Figure S7).

### Benefit of AI-assisted radiologist delineations

Both models showed a significant gain in segmenting omental implants when trained with full and AI-assisted labels compared to training with partially labeled cohorts (SMIT  $p = 0.015$ , Swin UNETR  $p = 0.017$ ). Precision (SMIT  $p = 0.04$ , Swin UNETR  $p = 0.020$ ) and recall (SMIT  $p = 0.04$ , Swin UNETR  $p = 0.038$ ) also improved for detecting omental implants when the models were trained with full and AI assisted labels. SMIT was significantly more accurate compared to Swin UNETR when trained with full and partially labeled examples (DSC  $p = 0.015$ , precision  $p = 0.04$ ). Figure 4 shows a representative example from the testing set with improved segmentations produced by both methods when trained with AI-assisted labels.

AI-assisted labeling improved to correct missing delineation of omental implants in 72 out of 245 cases. Radiologist edits were required for fewer voxels when using AI segmentations (APL median of 39.55 and IQR of 10.41 to 63.13) compared to radiologist corrections to preliminary partial delineations (APL median of 106.49, IQR of 55.22 to 208.44). Supplementary Figure S8 shows representative examples with initial partial segmentations with missing segmentations of omental implants, the AI generated segmentation, and the radiologist delineations using the results of AI segmentations.

### Quantifying organs overlap with tumor segmentation

Finally, we measured the organs where false detections and segmentations occurred for the two methods. We focused on the colon, small bowel, and urinary bladder because the analyzed tumors occurred in close spatial proximity to these organs. SMIT resulted in a comparably smaller proportion of false detections in the small bowel, colon, and the urinary bladder compared to Swin UNETR (Table 4 and Figure 5), indicating that Swin UNETR resulted in over-segmentations on the testing set.

## Discussion

In this study, we presented the first application of two transformer-based AI methods to segment adnexal masses and omental implants in patients with HGSOE. One prior study [18] applied to ovarian metastases segmentation focused on perihepatic and perisplenic tumors, both of which have a hypodense appearance on the CT using non-deep learning method. Another study employed nnU-Net framework to generate segmentation of the primary tumor and omental implants [19], the same tumor types evaluated in our study. Our study used a transformer-based encoder followed by a convolutional decoder network, pretrained the encoder with a large corpus of medical scans and evaluated the feasibility to use partially annotated examples to generate high quality segmentations.

Both transformer methods produced reasonably accurate segmentations, especially when using AI-assisted segmentations. However, the individual methods differed in precision and recall rates with SMIT providing significantly higher precision compared to the Swin UNETR model, especially for omental implants. SMIT generated a smaller proportion of false detections of tumors within normal tissues such as the small bowel, the colon, and the urinary bladder than the Swin UNETR method.

We, for the first time, also studied the utility of AI-assisted labels in improving AI model accuracy. Our analysis showed that both models resulted in significant accuracy improvement particularly for hard to segment multifocal omental implants. These results indicate that using AI-assisted delineations to improve partial label segmentations can reduce the radiologist effort needed for careful delineation of tumors on every slice. We applied this approach in only a single round of improvement and training, whereby the AI-assisted labeling was performed only once following training with partial labels. It is conceivable that similar methods could be useful with even fewer annotations in an active learning framework as a part of future studies.

Both AI models were trained on institutional dataset and then evaluated on the public Cancer Imaging Archive dataset consisting of images sourced from multiple institutions and different scanner manufacturers (GE, Siemens, Philips, and Toshiba) to ensure generalization capability of these methods. However, we did not perform an evaluation of the accuracy variations across the scanner manufacturers due to limited sample size, wherein most scans used GE, followed by Siemens, and a handful of scans using Phillips and Toshiba scanners. Finally, we only considered implants in the omentum in addition to adnexal tumors due to the practical limitations in producing carefully curated radiologist delineations of additional metastatic sites.

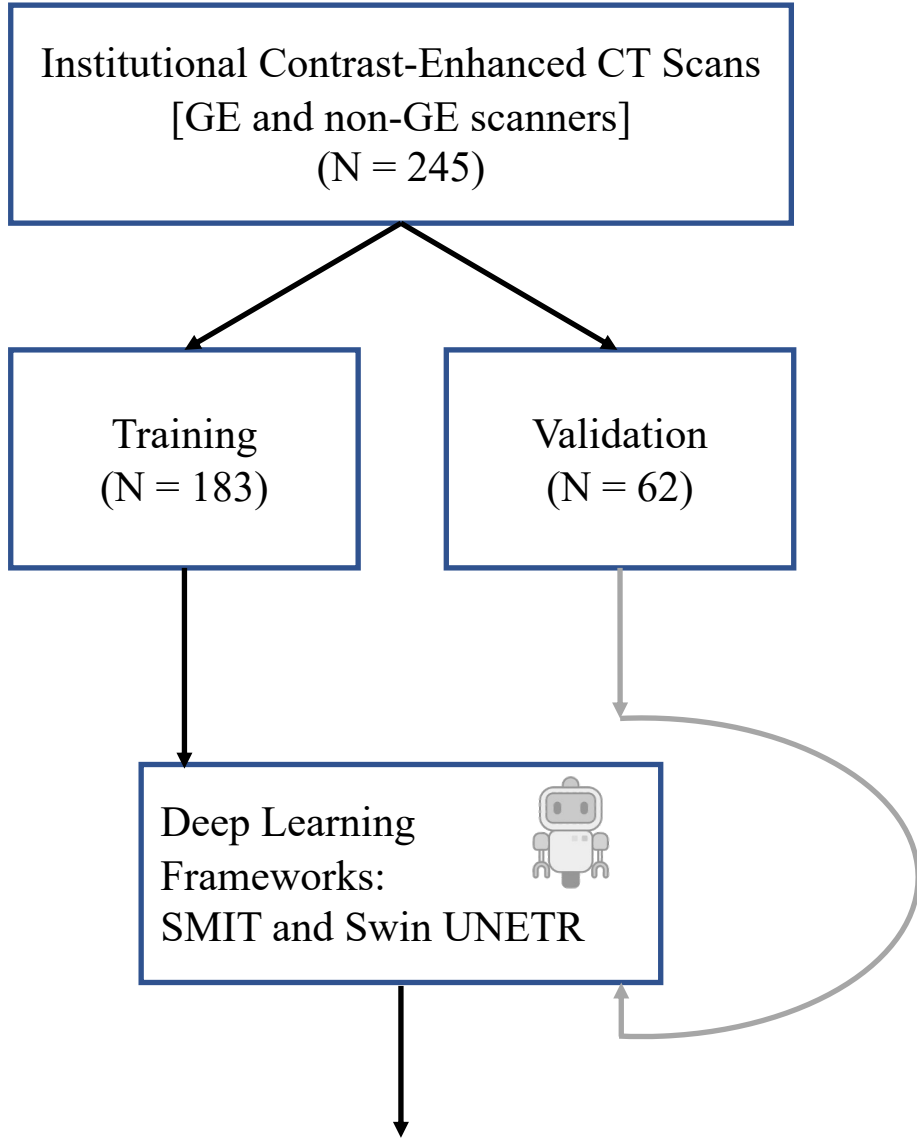
Nevertheless, this is the first study to our best knowledge that demonstrates the capability of transformer-based AI models to segment ovarian cancer lesions and achieves reasonably accurate segmentations for the detected tumors especially when using an AI-assisted labeling framework. Potential clinical applications are a more accurate assessment of overall disease volume, especially given the challenge of assessing peritoneal disease. This is particularly relevant when measuring response to treatment on clinical trials, with future capability to augment the traditional RECIST infrastructure.

## References

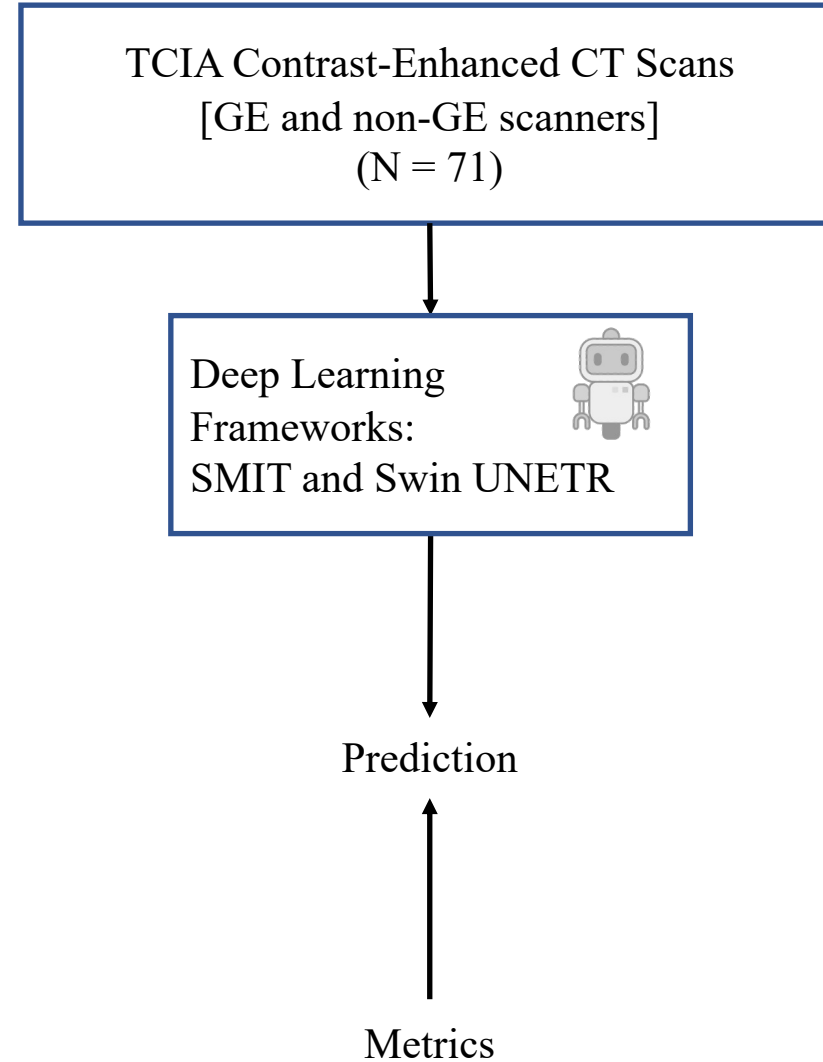
1. Siegel RL, Giaquinto AN, Jemal A. Cancer statistics, 2024. *CA Cancer J Clin.* 2024;74(1):12–49. DOI: 10.3322/caac.21820
2. Bristow RE, Tomacruz RS, Armstrong DK, Trimble EL, Montz FJ. Survival effect of maximal cytoreductive surgery for advanced ovarian carcinoma during the platinum era: a meta-analysis. *J Clin Oncol.* 2002;20(5):1248–1259. DOI: 10.1200/JCO.2002.20.5.1248
3. Chang SJ, Bristow RE, Chi DS, Cliby WA. Role of aggressive surgical cytoreduction in advanced ovarian cancer. *J Gynecol Oncol.* 2015;26(4):336–342. DOI: 10.3802/jgo.2015.26.4.336
4. Chiva L, Lapuente F, Castellanos T, Alonso S, Gonzalez-Martin A. What Should We Expect After a Complete Cytoreduction at the Time of Interval or Primary Debulking Surgery in Advanced Ovarian Cancer? *Ann Surg Oncol.* 2016;23(5):1666–1673. DOI: 10.1245/s10434-015-5051-9
5. Jayson GC, Kohn EC, Kitchener HC, Ledermann JA. Ovarian cancer. *Lancet.* 2014;384(9951):1376–1388. DOI: 10.1016/S0140-6736(13)62146-7
6. Burrell RA, Swanton C. Tumour heterogeneity and the evolution of polyclonal drug resistance. *Mol Oncol.* 2014;8(6):1095–1111. DOI: 10.1016/j.molonc.2014.06.005
7. Greaves M, Maley CC. Clonal evolution in cancer. *Nature.* 2012;481(7381):306–313. DOI: 10.1038/nature10762
8. Cooke SL, Brenton JD. Evolution of platinum resistance in high-grade serous ovarian cancer. *Lancet Oncol.* 2011;12(12):1169–1174. DOI: 10.1016/S1470-2045(11)70123-1
9. Bashashati A, Ha G, Tone A, et al. Distinct evolutionary trajectories of primary high-grade serous ovarian cancers revealed through spatial mutational profiling. *J Pathol.* 2013;231(1):21–34. DOI: 10.1002/path.4230
10. McPherson A, Roth A, Laks E, et al. Divergent modes of clonal spread and intraperitoneal mixing in high-grade serous ovarian cancer. *Nat Genet.* 2016;48(7):758–767. DOI: 10.1038/ng.3573
11. Jiménez-Sánchez A, Memon D, Pourpe S, et al. Heterogeneous Tumor-Immune Microenvironments among Differentially Growing Metastases in an Ovarian Cancer Patient. *Cell.* 2017;170(5):927–938.e20. DOI: 10.1016/j.cell.2017.07.025
12. Zhang AW, McPherson A, Milne K, et al. Interfaces of Malignant and Immunologic Clonal Dynamics in Ovarian Cancer. *Cell.* 2018;173(7):1755–1769.e22. DOI: 10.1016/j.cell.2018.03.073
13. Langlotz CP, Allen B, Erickson BJ, et al. A Roadmap for Foundational Research on Artificial Intelligence in Medical Imaging: From the 2018 NIH/RSNA/ACR/The Academy Workshop. *Radiology.* 2019;291(3):781–791. DOI: 10.1148/radiol.2019190613
14. Jiang J, Rimner A, Deasy JO, Veeraraghavan H. Unpaired cross-modality educed distillation (CMEDL) for medical image segmentation. *IEEE Trans Med Imaging.* 2021;PP. DOI: 10.1109/TMI.2021.3132291.
15. Robinson-Weiss C, Patel J, Bizzo BC, et al. Machine Learning for Adrenal Gland Segmentation and Classification of Normal and Adrenal Masses at CT. *Radiology.* 2023;306(2):e220101. DOI: 10.1148/radiol.220101
16. Chen P-T, Wu T, Wang P, et al. Pancreatic Cancer Detection on CT Scans with Deep Learning: A Nationwide Population-based Study. *Radiology.* 2023;306(1):172–182. DOI: 10.1148/radiol.220152
17. Vorontsov E, Cerny M, Régnier P, et al. Deep Learning for Automated Segmentation of Liver Lesions at CT in Patients with Colorectal Cancer Liver Metastases. *Radiol Artif Intell.* 2019;1(2). DOI: 10.1148/ryai.2019180014



18. Liu J, Wang S, Linguraru MG, Yao J, Summers RM. Tumor sensitive matching flow: A variational method to detecting and segmenting perihepatic and perisplenic ovarian cancer metastases on contrast-enhanced abdominal CT. *Med Image Anal.* 2014;18(5):725–739. DOI: 10.1016/j.media.2014.04.001
19. Buddenkotte T, Rundo L, Woitek R, et al. Deep learning-based segmentation of multisite disease in ovarian cancer. *Eur Radiol Exp.* 2023;7(1):77. DOI: 10.1186/s41747-023-00388-z
20. Cao H, Wang Y, Chen J, et al. Swin-Unet: Unet-Like Pure Transformer for Medical Image Segmentation. *Computer Vision – ECCV 2022 Workshops.* Springer Nature Switzerland; 2023. p. 205–218. DOI: 10.1007/978-3-031-25066-8\_9
21. Sobirov I, Nazarov O, Alasmawi H, Yaqub M. Automatic Segmentation of Head and Neck Tumor: How Powerful Transformers Are? *arXiv [eess.IV]*. 2022. <http://arxiv.org/abs/2201.06251>.
22. Rangnekar A, Nadkarni N, Jiang J, Veeraraghavan H. Trustworthiness of Pretrained Transformers for Lung Cancer Segmentation. *arXiv [eess.IV]*. 2024. <http://arxiv.org/abs/2403.13113>.
23. Jiang J, Tyagi N, Tringale K, Crane C, Veeraraghavan H. Self-supervised 3D anatomy segmentation using self-distilled masked image transformer (SMIT). *Med Image Comput Comput Assist Interv.* 2022;13434:556–566. DOI: 10.1007/978-3-031-16440-8\_53
24. Willemink MJ, Roth HR, Sandfort V. Toward Foundational Deep Learning Models for Medical Imaging in the New Era of Transformer Networks. *Radiol Artif Intell.* 2022;4(6). DOI: 10.1148/ryai.210284
25. Tang Y, Yang D, Li W, et al. Self-Supervised Pre-Training of Swin Transformers for 3D Medical Image Analysis. *2022 IEEE/CVF Conference on Computer Vision and Pattern Recognition (CVPR).* IEEE; 2022. p. 20698–20708. DOI: 10.1109/CVPR52688.2022.02007
26. Jiang J, Hu Y-C, Liu C-J, et al. Multiple Resolution Residually Connected Feature Streams for Automatic Lung Tumor Segmentation From CT Images. *IEEE Trans Med Imaging.* 2019;38(1):134–144. DOI: 10.1109/TMI.2018.2857800
27. Boehm, K.M., Aherne, E.A., Ellenson, L., Nikolovski, I., Alghamdi, M., Vázquez-García, I., Zamarin, D., Long Roche, K., Liu, Y., Patel, D. and Aukerman, A., 2022. Multimodal data integration using machine learning improves risk stratification of high-grade serous ovarian cancer. *Nature cancer*, 3(6), pp.723-733. DOI: 10.1038/s43018-022-00388-9
28. Vargas HA, Huang EP, Lakhman Y, et al. Radiogenomics of High-Grade Serous Ovarian Cancer: Multireader Multi-Institutional Study from the Cancer Genome Atlas Ovarian Cancer Imaging Research Group. *Radiology.* 2017;285(2):482–492. DOI: 10.1148/radiol.2017161870
29. Liu Z, Lin Y, Cao Y, et al. Swin Transformer: Hierarchical Vision Transformer using Shifted Windows. *2021 IEEE/CVF International Conference on Computer Vision (ICCV).* IEEE; 2021. p. 9992–10002. DOI: 10.1109/ICCV48922.2021.00986
30. Ronneberger O, Fischer P, Brox T. U-Net: Convolutional Networks for Biomedical Image Segmentation. *arXiv [cs.CV]*. 2015. <http://arxiv.org/abs/1505.04597>. DOI: 10.1007/978-3-319-24574-4\_28
31. Tarvainen A, Valpola H. Mean teachers are better role models: Weight-averaged consistency targets improve semi-supervised deep learning results. *Proceedings of the 31st International Conference on Neural Information Processing Systems.* Red Hook, NY, USA: Curran Associates Inc.; 2017. p. 1195–1204.
32. Vaassen F, Hazelaar C, Vaniqui A, et al. Evaluation of measures for assessing time-saving of automatic organ-at-risk segmentation in radiotherapy. *Phys Imaging Radiat Oncol.* 2020;13:1–6. DOI: 10.1016/j.phro.2019.12.001
33. Wasserthal J, Breit H-C, Meyer MT, et al. TotalSegmentator: Robust Segmentation of 104 Anatomic Structures in CT

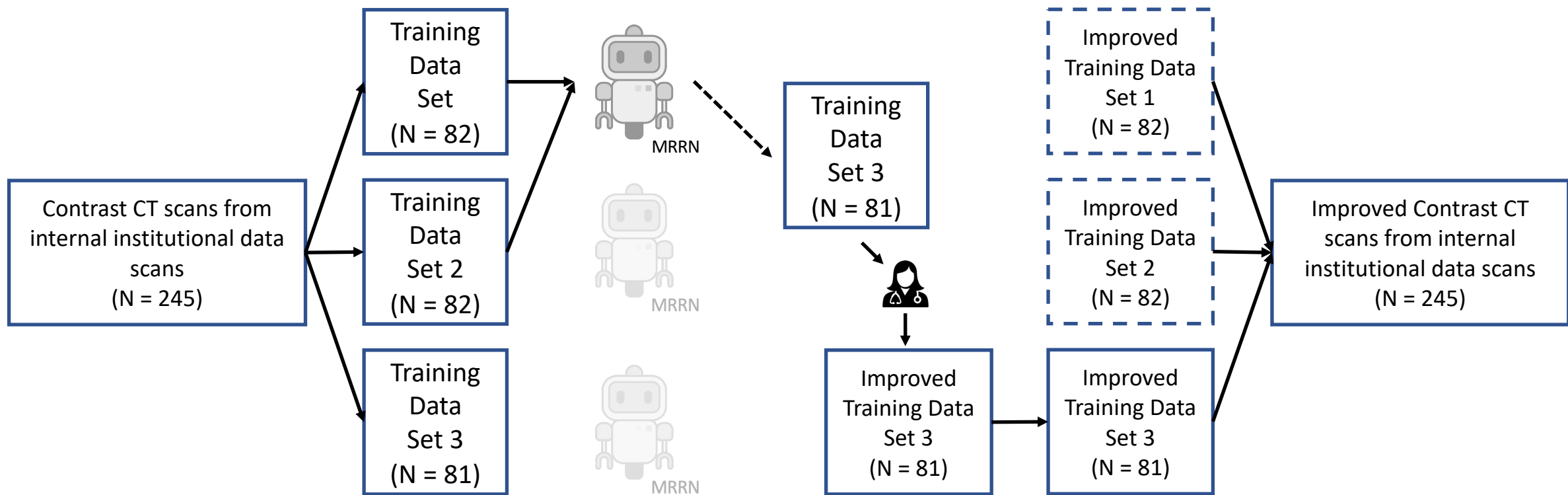


(a) Fine-tuning training



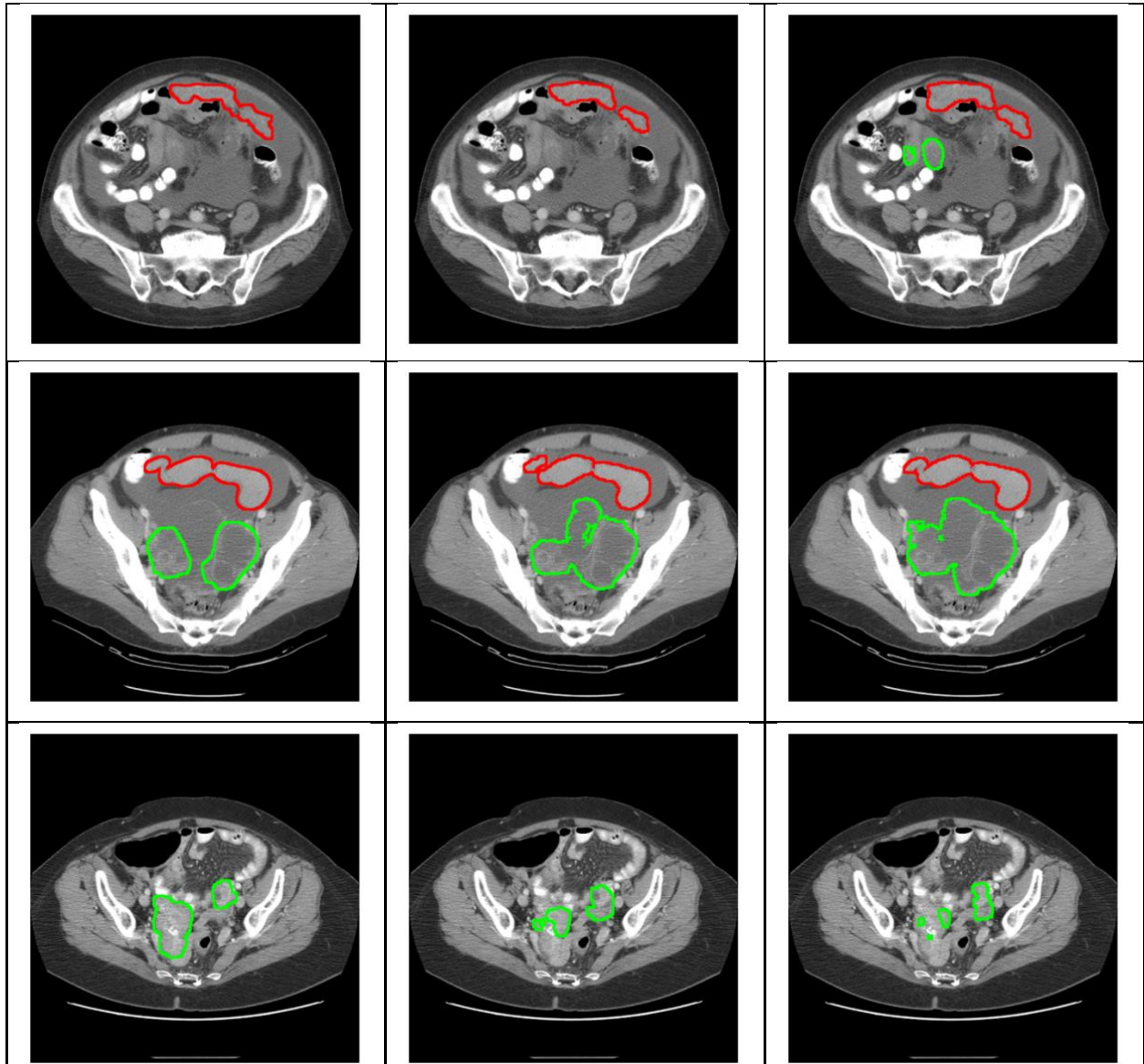
(b) Fine-tuning evaluation

Figure 1. Summary Algorithm Framework



(c) AI-assisted labeling using the MRRN model

Figure 1. Summary Algorithm Framework

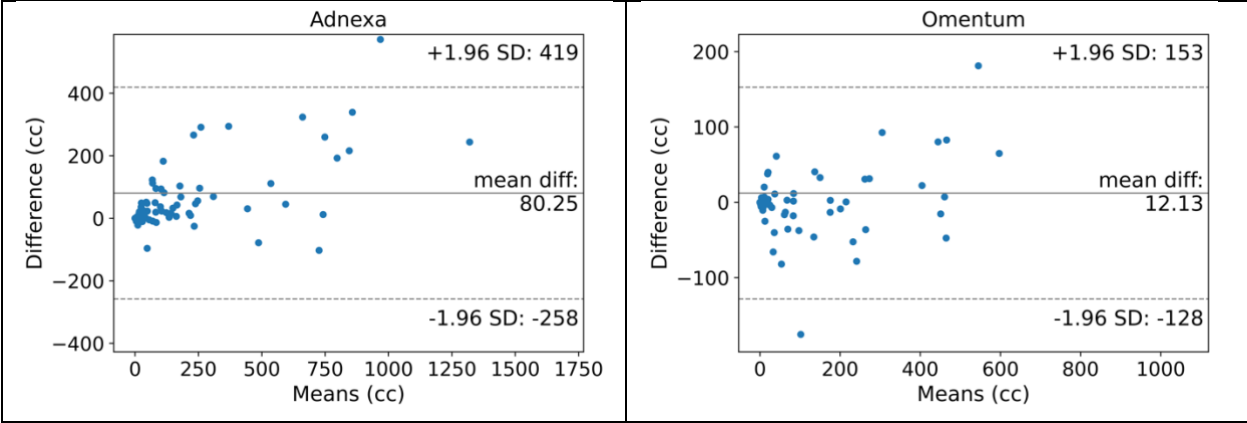


(A) Expert delineation

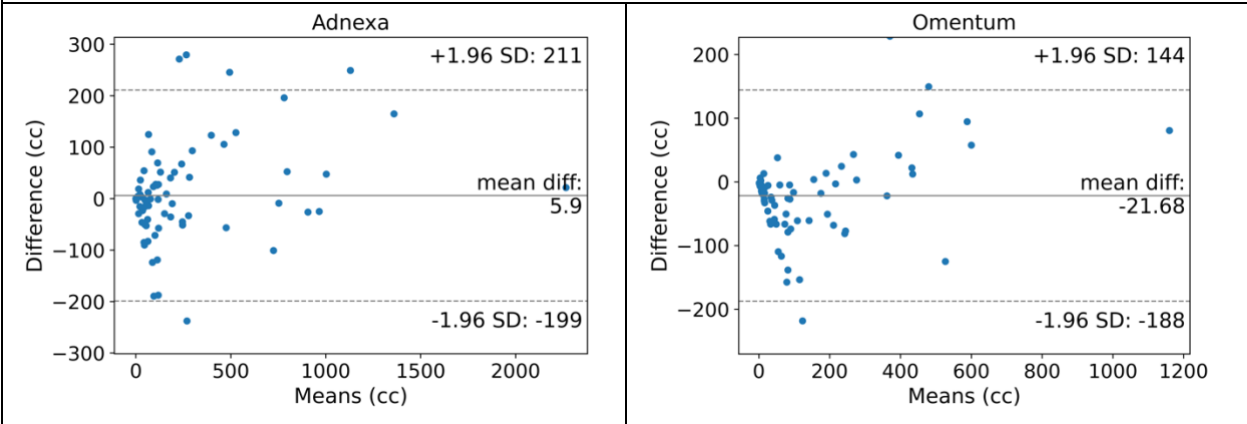
(B) SMIT

(C) Swin UNETR

Figure 2. Segmentations produced on representative cases by the SMIT and Swin UNETR models, with the expert delineation. Red and green contours represent omental and adnexal tumors, respectively.

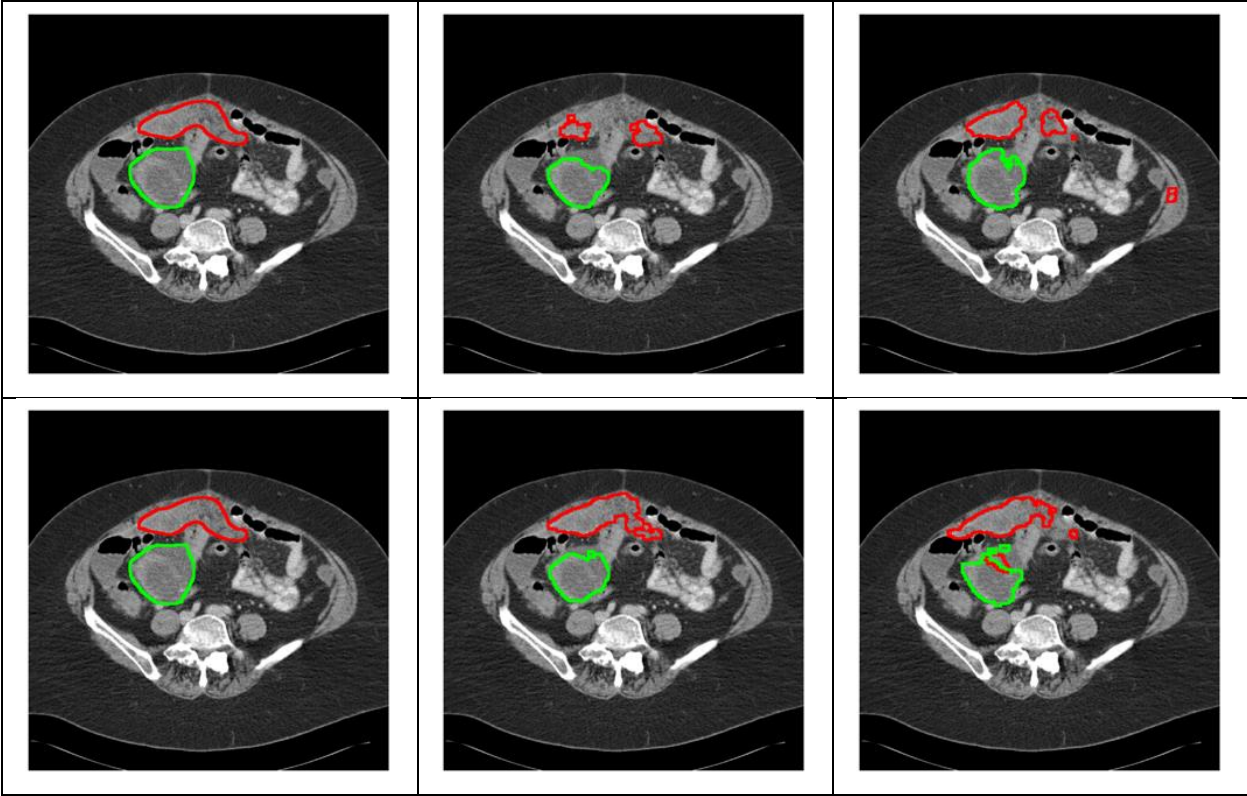


(a) SMIT



(b) Swin UNETR

Figure 3. Bland-Altman Plots of manual delineations versus model predictions. The x-axis depicts  $(\text{manual delineation} + \text{AI segmentation})/2$  and the y-axis depicts  $(\text{manual delineations} - \text{AI segmentation})/2$ .

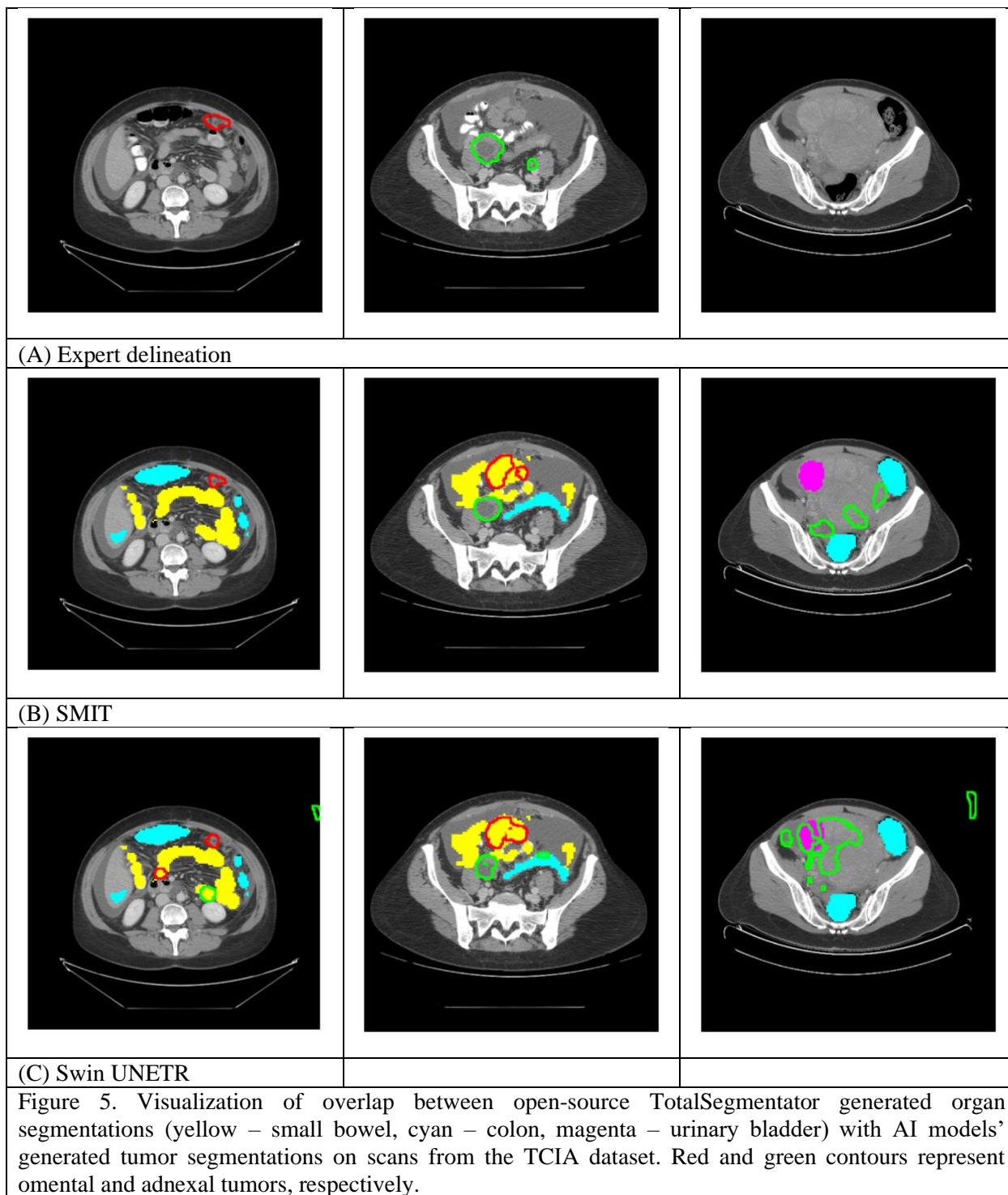


(A) Expert delineation

(B) SMIT

(C) Swin UNETR

Figure 4. Representative example from the testing set with expert delineation, segmentation produced by SMIT and Swin UNETR when trained with partial labeled examples (top row) and AI-assisted radiologist delineations examples (bottom row). Red and green contours represent omental and adnexal tumors, respectively.



## Tables

Table 1: Training/Validation/Test sets distributions. Median and Interquartile range (IQR) is shown as 'IQR:' where applicable.

	Training (Institutional)	Validation (Institutional)	Test/Evaluation (Public – TCIA)
Number of scans	183	62	71
Lesion Volume in Adnexa (cc)	32.33 [IQR: 6.32 to 723.54]	58.88 [IQR: 3.37 to 750.32]	129.73 [IQR: 35.47 to 323.07]
Lesion Volume in Omentum (cc)	52.62 [IQR: 9.39 to 392.70]	43.65 [IQR: 6.21 to 200.01]	37.90 [IQR: 1.87 to 200.1]
Voxel Spacing (mm)	2.5 – 5.0	2.5 – 5.0	2.0 – 10.0
Scanners: GE	125	45	43
Scanners: Non-GE	58	17	28
Axial-plane resolution (mm)	0.80 [IQR: 0.72, 0.86]	0.79 [IQR: 0.75, 0.87]	0.76 [IQR: 0.70, 0.82]
Slice thickness (mm)	5.0 [2.5, 5.0]	5.0 [2.5, 5.0]	5.0 [1.0, 10.0]
KVp (mA)	120 [80, 140]	120 [100, 130]	120 [100, 140]



Table 2: Training and evaluation hyperparameters for SMIT and Swin UNETR models.

System	Ubuntu 18.05.5 LTS
GPU	Nvidia A100 80 GB x 4 (training), x 1 (evaluation)
Programming language	Python 3.8
Deep learning framework and tools	Pytorch 1.13 ( <a href="https://doi.org/10.48550/arXiv.1912.01703">doi.org/10.48550/arXiv.1912.01703</a> ), MONAI ( <a href="https://doi.org/10.48550/arXiv.2211.02701">doi.org/10.48550/arXiv.2211.02701</a> ), SimpleITK, Nibabel
Batch size	4
Patch Size	128 x 128 x 128 (SMIT), 96 x 96 x 96 (Swin UNETR)
Normalization	[-175,250]
Total Epochs	1000
Learning Rate	2e-4
Learning Rate Decay	Linear Warmup with Cosine Annealing
Loss Functions	Cross-Entropy with Dice Loss
Evaluation Augmentation	50% Sliding window overlap

Table 3: Testing accuracy in terms of DSC, ASSD, Precision and Recall on the models.

Tumor	SMIT				Swin UNETR			
	DSC	ASSD (mm)	Precision	Recall	DSC	ASSD (mm)	Precision	Recall
Adnexa								
Full and partial labels	0.82 ± 0.05	2.55 ± 1.62	0.45	0.59	0.78 ± 0.14	3.62 ± 4.50	0.24	0.58
Full and AI-assisted labels	0.81 ± 0.08	2.62 ± 1.74	0.52	0.60	0.77 ± 0.16	3.56 ± 4.66	0.22	0.62
Omental Metastases								
Full and partial labels	0.73 ± 0.09	2.64 ± 1.71	0.14	0.30	0.73 ± 0.09	2.54 ± 1.95	0.05	0.31
Full and AI-assisted labels	0.76 ± 0.12	2.12 ± 2.67	0.25	0.59	0.75 ± 0.10	3.22 ± 4.39	0.11	0.50

Table 4: False tumor predictions within healthy organs produced by evaluated networks (cc). Median and Interquartile range (IQR) is shown. Statistical test was performed using pairwise, two-sided, Wilcoxon signed rank test comparing SMIT and Swin UNETR networks.

False predictions within organs	Adnexa			Omental Metastases		
	SMIT	Swin UNETR	p-value	SMIT	Swin UNETR	p-value
Small Bowel	0.01 [0.00 to 0.57]	1.13 [0.03 to 5.24]	< 0.001	2.16 [0.04 to 9.66]	7.37 [1.86 to 23.90]	0.001
Colon	0.00 [0.00 to 0.07]	0.08 [0.00 to 0.65]	0.001	0.27 [0.00 to 1.81]	1.34 [0.10 to 5.35]	0.001
Urinary Bladder	0.00 [0.00 to 0.10]	0.00 [0.00 to 1.30]	0.09	0.00 [0.00 to 0.00]	0.00 [0.00 to 0.00]	0.39

Supplemental Material

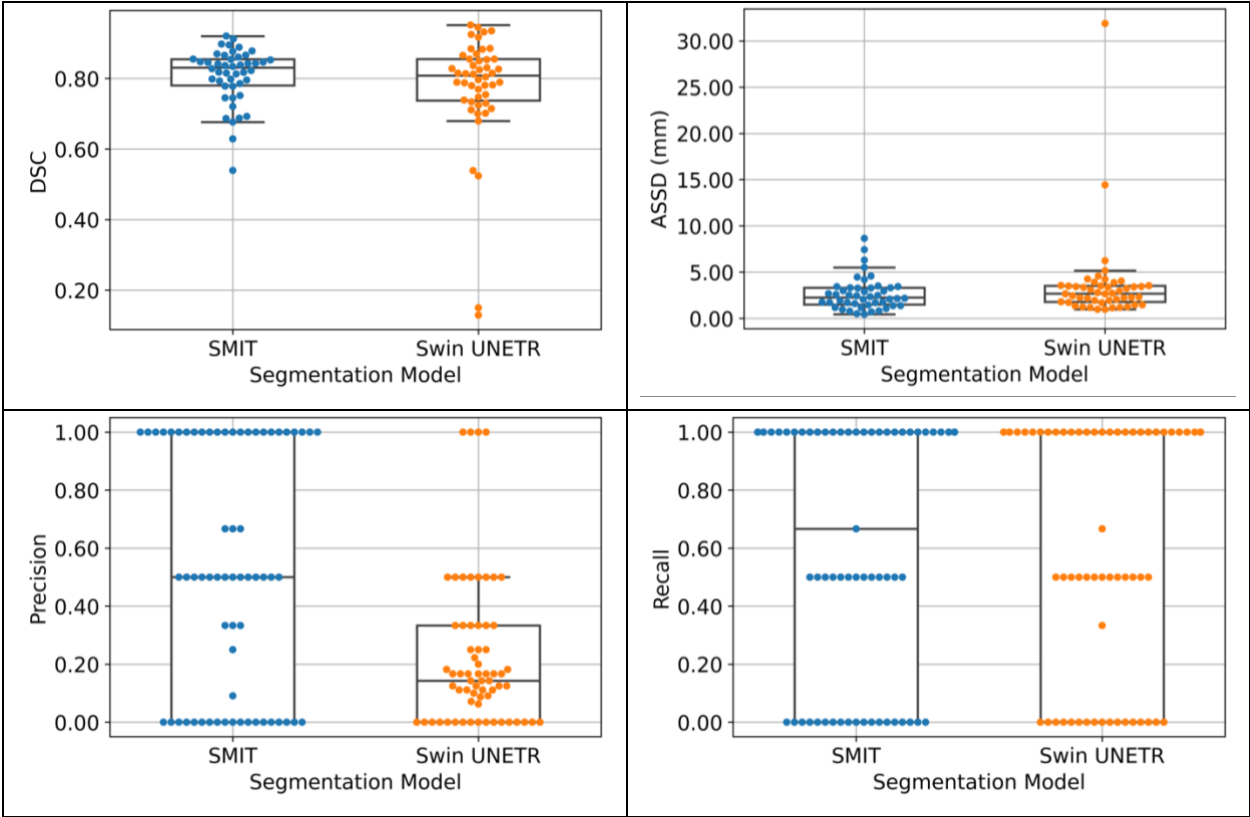


Figure S1. Tumor-specific segmentation accuracy for all evaluated (testing set) tumors in the adnexa shows that SMIT resulted in reduced spread compared to Swin UNETR with DSC.

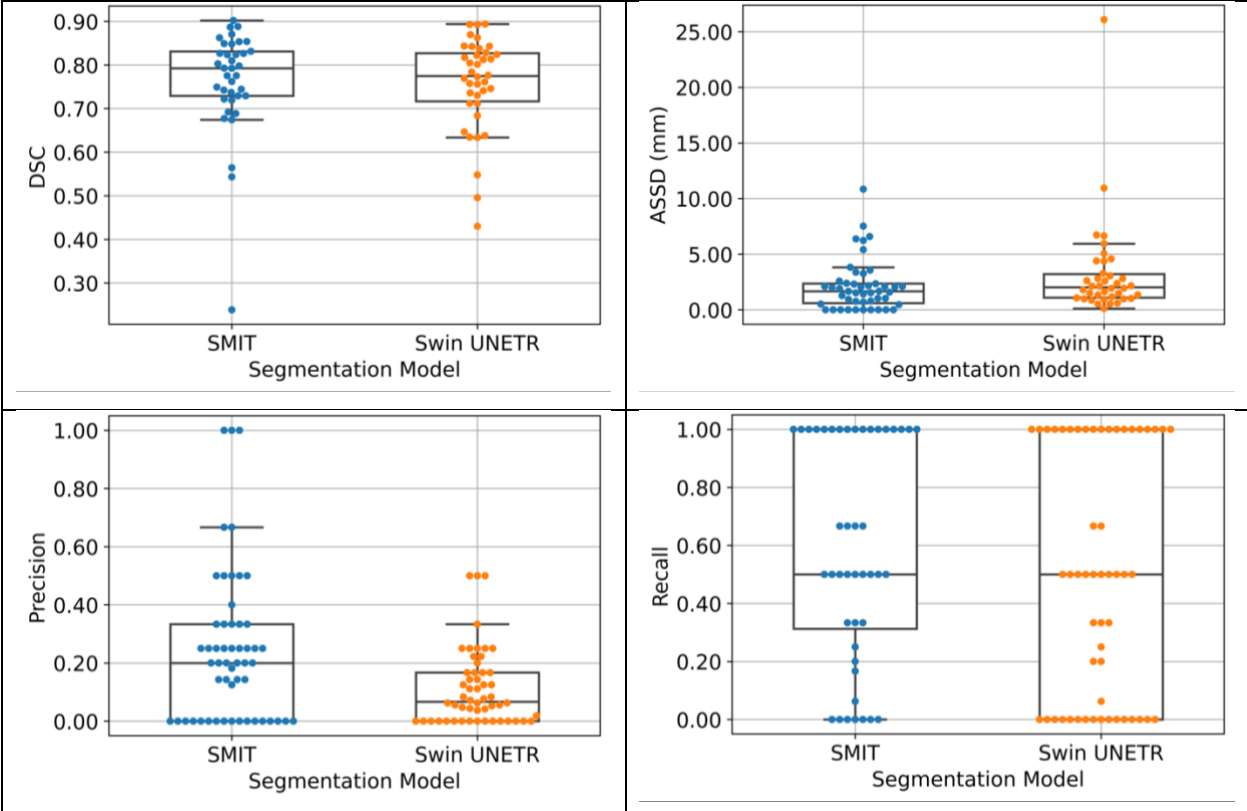


Figure S2. Tumor-specific segmentation accuracy for all evaluated (testing set) tumors in the omentum shows that SMIT resulted in reduced spread compared to Swin UNETR with DSC.

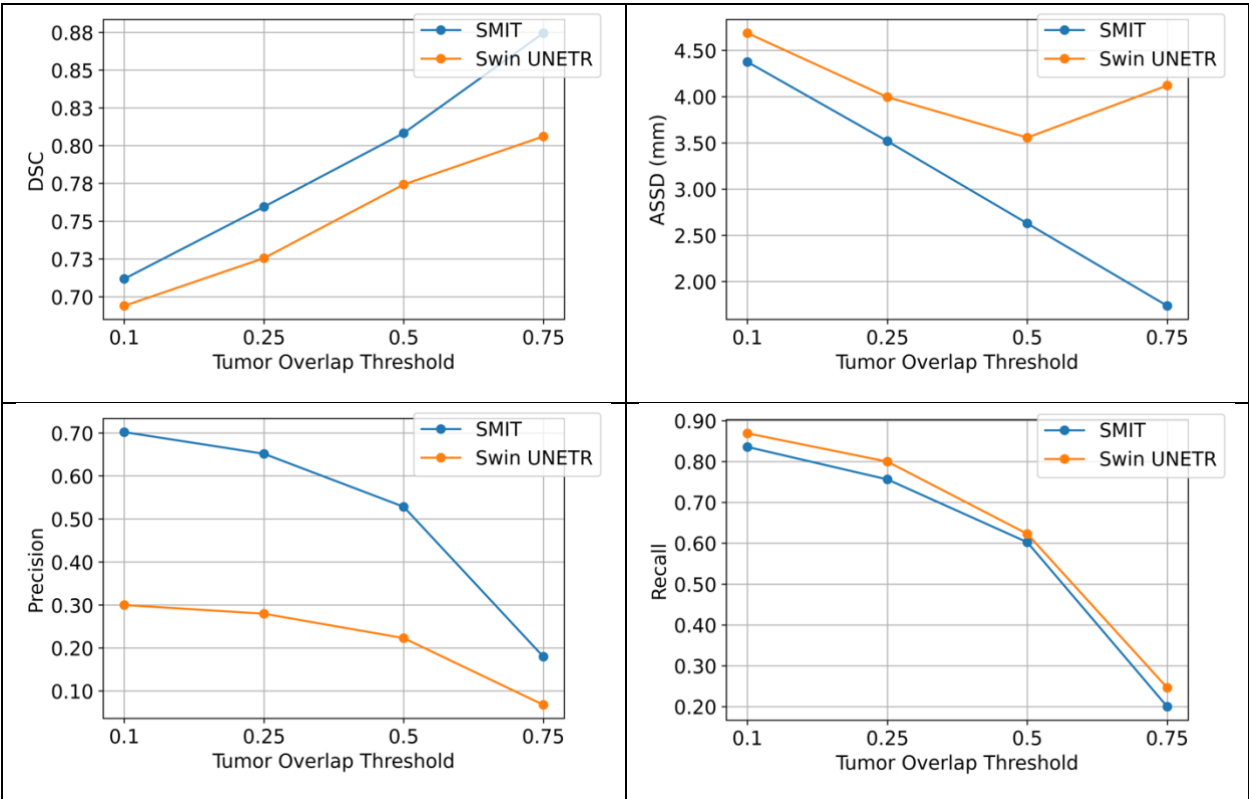


Figure S3. Calibration curve for tumors in the adnexa computed for multiple metrics including DSC, ASSD, Precision, and Recall show that SMIT resulted in higher accuracy than Swin UNETR for all the tumor detection thresholds.

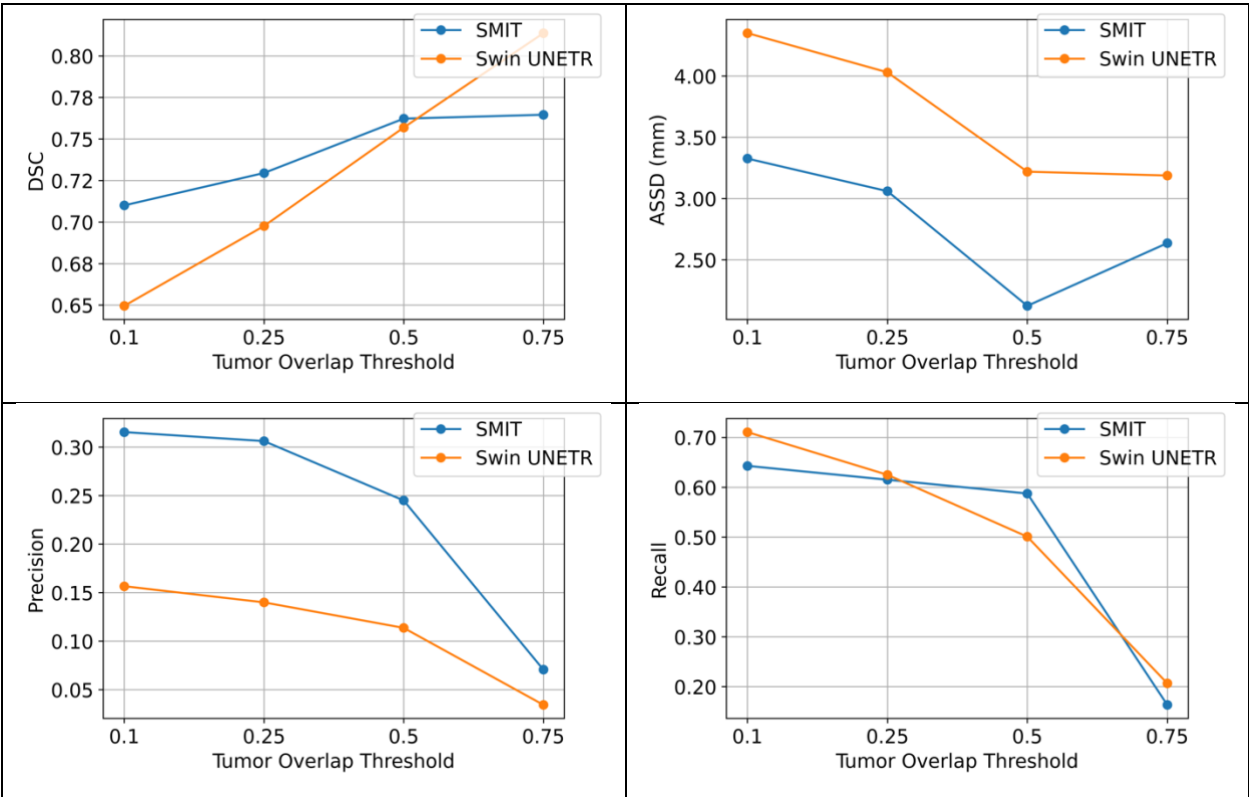
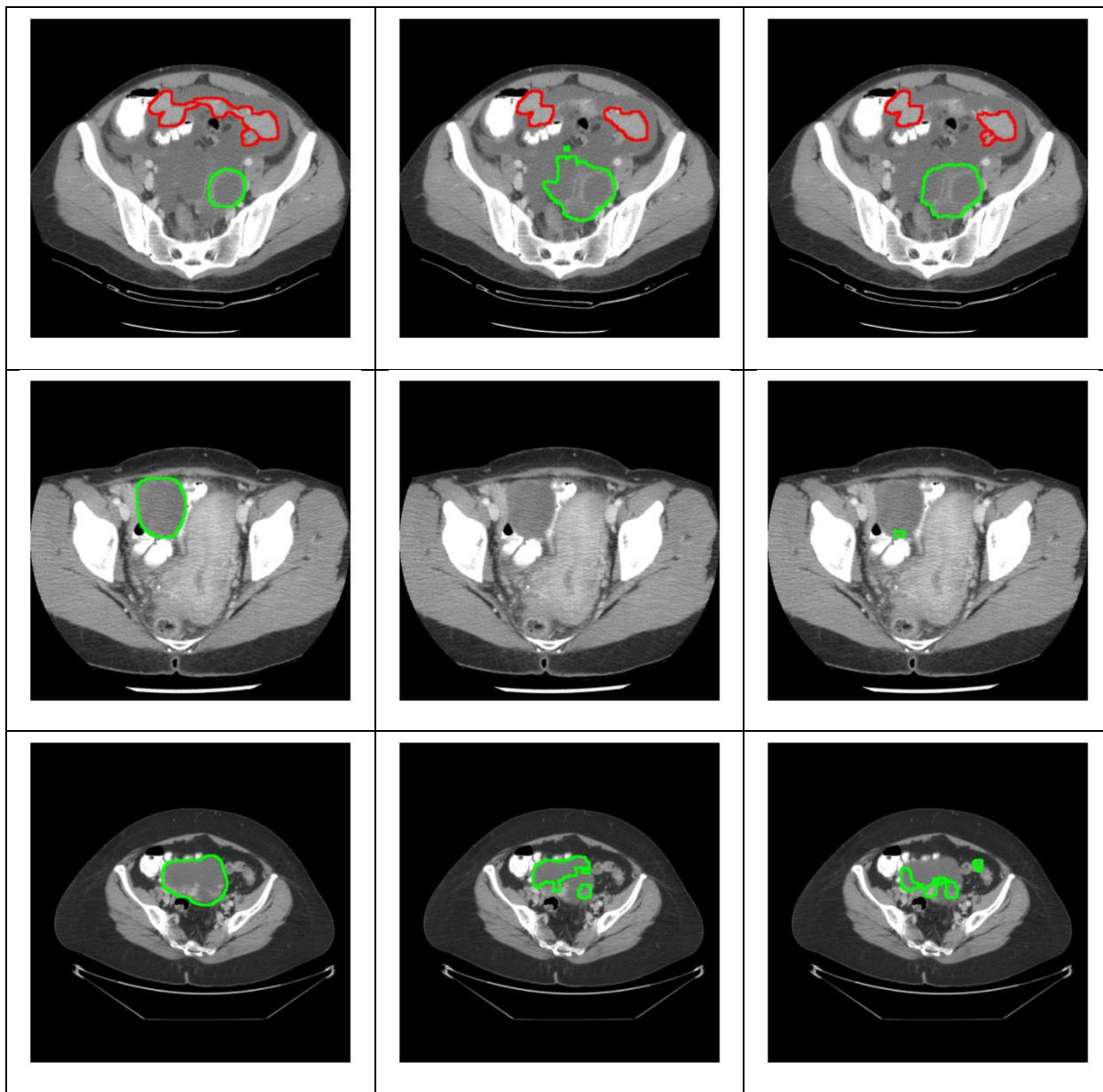


Figure S4. Calibration curve for tumors in the omentum computed for multiple metrics including DSC, ASSD, Precision, and Recall show that SMIT resulted in higher accuracy than Swin UNETR for all the tumor detection thresholds.



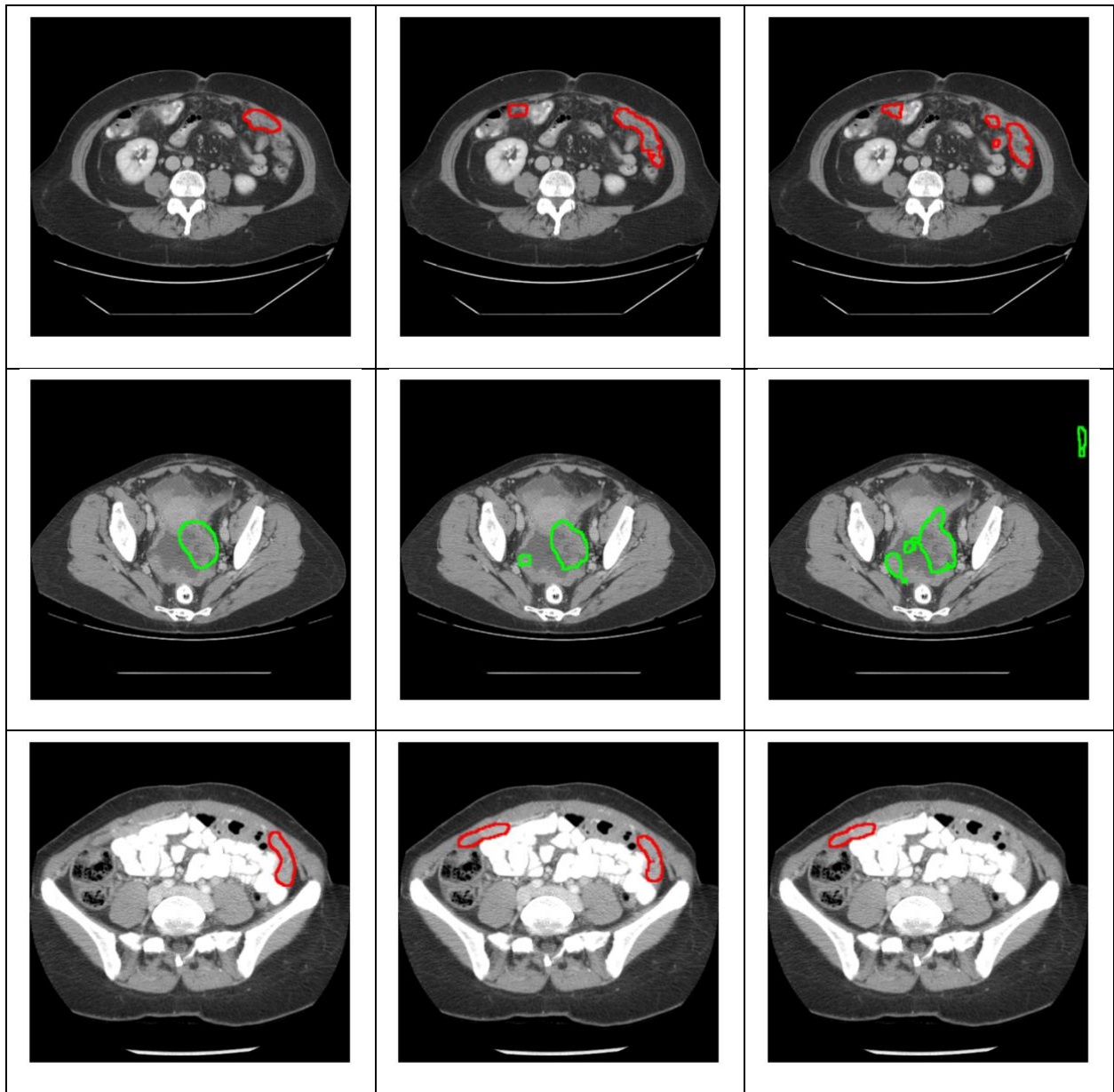
(A) Manual delineations

(B) SMIT

(C) Swin UNETR

Figure S5. Cases within the TCIA dataset with missed AI segmentations. Red and green contours represent omental and adnexal tumors, respectively.



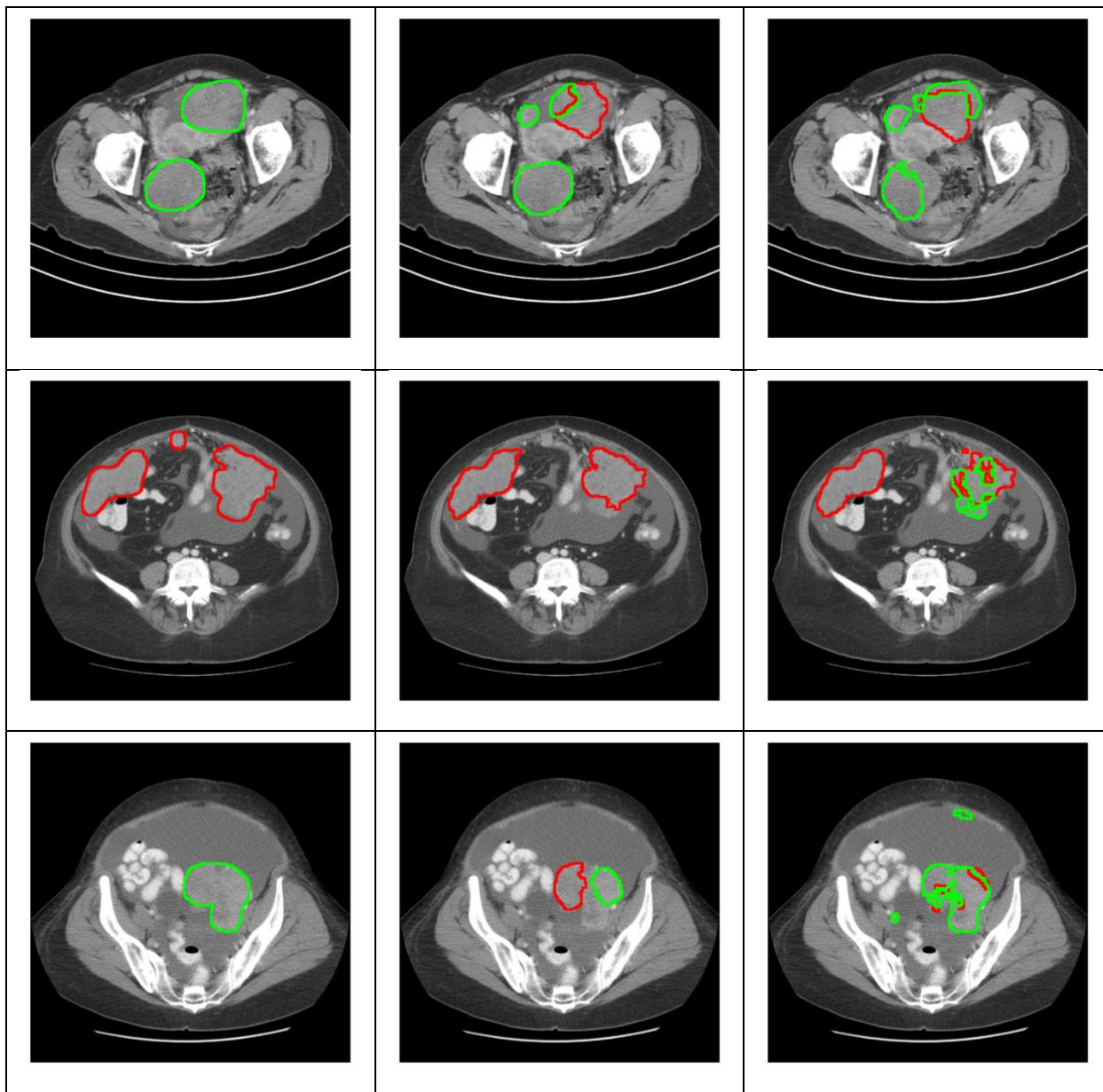


(A) Manual delineations

(B) SMIT

(C) Swin UNETR

Figure S6. Cases within the TCIA dataset with additional segmentations. Red and green contours represent omental and adnexal tumors, respectively.



(A) Manual delineations

(B) SMIT

(C) Swin UNETR

Figure S7. Cases within the TCIA dataset with mislabel tumor class segmentations. Red and green contours represent omental and adnexal tumors, respectively.

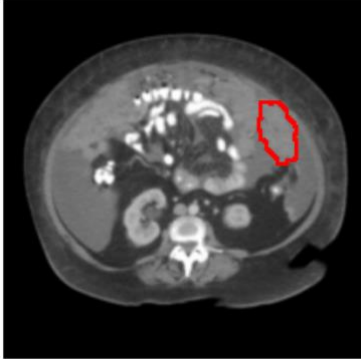
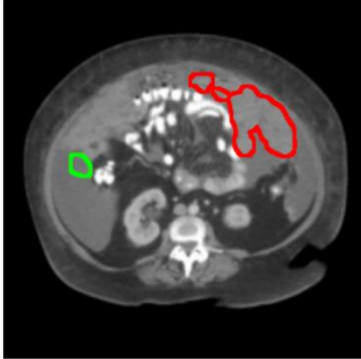

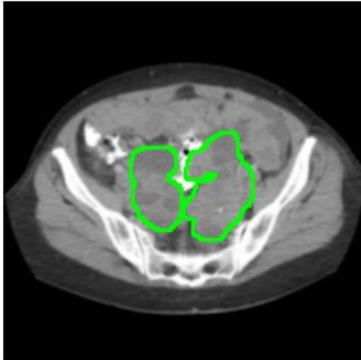
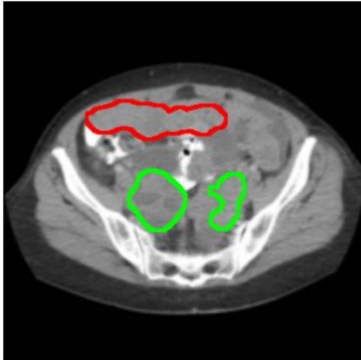

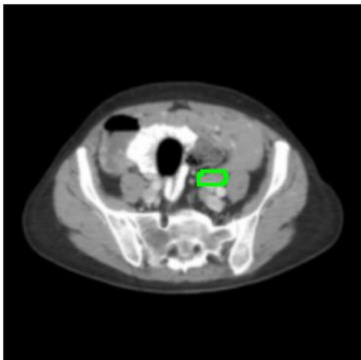
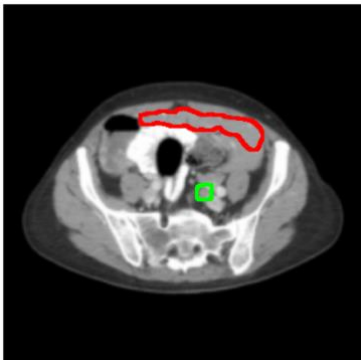
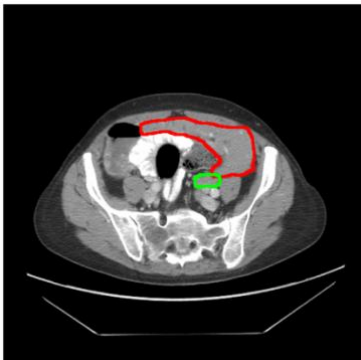
		
		
		
(A) Initial partial delineations	(B) AI-generated segmentations	(C) AI-assisted radiologist delineations

Figure S8. Representative cases showcasing initial partial segmentations with missing segmentations of the metastatic lesions in the omentum, the AI generated segmentation, and the radiologist delineations using the results of AI segmentations. Red and green contours represent omental and adnexal tumors, respectively.